

# Optic Disk and Cup Segmentation from Monocular Colour Retinal Images for Glaucoma Assessment

Gopal Datt Joshi, *Member, IEEE*, Jayanthi Sivaswamy, *Member, IEEE*, and S. R. Krishnadas

**Abstract**—Automatic retinal image analysis is emerging as an important screening tool for early detection of eye diseases. Glaucoma is one of the most common causes of blindness. The manual examination of optic disk (OD) is a standard procedure used for detecting glaucoma. In this paper, we present an automatic OD parameterization technique based on segmented OD and cup regions obtained from monocular retinal images. A novel OD segmentation method is proposed which integrates the local image information around each point of interest in multi-dimensional feature space to provide robustness against variations found in and around the OD region. We also propose a novel cup segmentation method which is based on anatomical evidence such as vessel bends at the cup boundary, considered relevant by glaucoma experts. Bends in a vessel are robustly detected using a region of support concept, which automatically selects the right scale for analysis. A multi-stage strategy is employed to derive a reliable subset of vessel bends called *r-bends* followed by a local spline fitting to derive the desired cup boundary. The method has been evaluated on 138 images comprising 33 normal and 105 glaucomatous images against three glaucoma experts. The obtained segmentation results show consistency in handling various geometric and photometric variations found across the dataset. The estimation error of the method for vertical cup-to-disk diameter ratio is 0.09/0.08 (mean/standard deviation) while for cup-to-disk area ratio it is 0.12/0.10. Overall, the obtained qualitative and quantitative results show effectiveness in both segmentation and subsequent OD parameterisation for glaucoma assessment.

**Index Terms**—Glaucoma, optic disk, cup, neuroretinal rim, segmentation, cup-to-disk ratio, active contour, vessel bend, retinal images.

## I. INTRODUCTION

GLAUCOMA is one of the common causes of blindness with about 79 million in the world likely to be afflicted with glaucoma by the year 2020 [1]. It is characterized by the progressive degeneration of optic nerve fibers and leads to structural changes of the optic nerve head, which is also referred to as optic disk, the nerve fiber layer and a simultaneous functional failure of the visual field. Since, glaucoma is asymptomatic in the early stages and the associated vision loss cannot be restored, its early detection and subsequent treatment is essential to prevent visual damage [2].

The optic disk (OD) is the location where ganglion cell axons exit the eye to form the optic nerve through which

visual information of the photo-receptors is transmitted to the brain. The OD can be divided into two distinct zones, namely, a central bright zone called the cup and a peripheral region called the neuroretinal rim where the nerve fibres bend into the cup region [3]. Major structures of the OD are shown in Fig. 1. The loss in optic nerve fibers leads to a change in the structural appearance of the OD, namely, the enlargement of cup region (thinning of neuroretinal rim) called cupping. Glaucoma detection typically considers the medical history, intra-ocular pressure and visual field loss tests of a patient together with a manual assessment of the OD, through ophthalmoscopy. Since enlargement of the cup with respect to OD is an important indicator of glaucoma progression, various parameters are estimated and recorded to assess the glaucoma stage. These include the diameter and area of OD, cup diameter, rim area, mean cup depth, etc. The subjectivity in the manual estimation of cup parameters is overcome, when possible, by using advanced modalities such as Optical Coherence Tomography and Heidelberg Retina Tomography. These provide the 3-D depth information either in the form of a colorless or pseudo-color image. The disk boundaries on the 3-D image are then manually marked by the experts to extract the desired disk parameters.

Colour fundus imaging (CFI) is another modality that can be used for glaucoma assessment. It has emerged as a preferred modality for large-scale retinal disease screening [4] and has already been established for large-scale diabetic retinopathy screening. It is possible to acquire fundus images in a non-invasive manner which is suitable for large scale screening. In such programs, an automated system that can decide whether or not any signs of suspicious for a disease are present in an image can improve efficiency; only those images deemed suspect by the system would require examination by an ophthalmologist.

There have been efforts to automatically detect glaucoma from 3-D images [5][6]. However, due to their high cost they are generally unavailable at primary care centers and hence a solution built around these imaging equipments is not appropriate for a large-scale screening program. Our work is aimed at developing a pre-screening system to enable glaucoma detection for large-scale screening programs using CFI. In this paper, we present partial results of this work.

Previously published work on automated glaucoma *detection* can be categorised into three main strategies: i) without disk parameterisation, ii) with disk parameterisation using *stereo* CFI, and iii) with disk parameterisation with *monocular* CFI. In the first category, a set of features are computed from the CFI and two-class classification is em-

Gopal Datt Joshi and Jayanthi Sivaswamy are with the Centre for Visual Information Technology, IIT Hyderabad, India, 500032. e-mail: gopal@research.iit.ac.in and jsivaswamy@iit.ac.in

S. R. Krishnadas is Chief Medical Officer at Aravind Eye Hospitals, Madurai, India. e-mail: krishnadas@aravind.org

Copyright (c) 2010 IEEE. Personal use of this material is permitted. However, permission to use this material for any other purposes must be obtained from the IEEE by sending a request to pubs-permissions@ieee.org.

Manuscript received October 01, 2010; revised December 06, 2010.

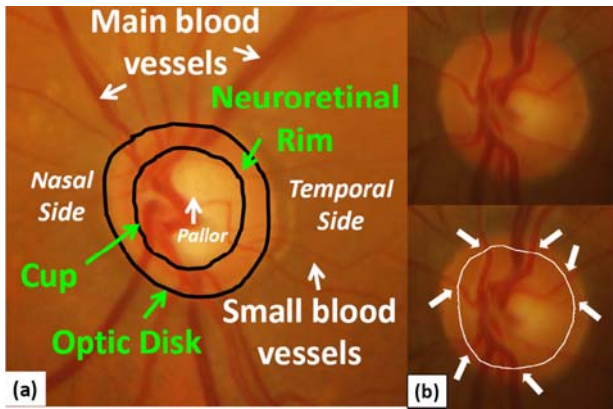


Fig. 1. a) A OD-centric monocular retinal image b) Cup boundary through vessel bends of interest.

ployed to declare a given image as normal or glaucomatous [7][8][9][3][10][11][12]. These features are computed at the image-level without performing OD and cup segmentation. Given the huge photometric and morphological variations presented by the OD, selection of features and classification strategy is difficult and challenging.

In the remaining class of strategies, which are based on disk parameterisation, OD and cup regions are segmented to estimate the relevant disk parameters. As against monocular CFI, a stereo set of CFI allows capture of partial depth information which helps in better characterising the region inside the OD such as the cup, neuroretinal rim. Considerable body of work in disk parameterisation has been carried out using stereo CFI [13][14][15][16][17][18]. However, only a handful attempts have been made to parameterise OD from monocular CFI. In this work, we focus on the parameterisation of OD from monocular images. Next, we describe the challenges associated with the problem and provide an overview of the related literature.

A monocular CFI gives a 2-D projection of retinal structures where OD appears as a bright circular or elliptic region partially occluded by blood vessels as shown in Fig. 1(a). Retinal nerve fibers converge to the OD and form a cup-shaped region known as the *cup*. Figure 1(a) highlights both regions. OD segmentation itself is a challenging task mainly due to blood vessel occlusions, ill-defined boundaries, image variations near the disk boundaries due to pathological changes and variable imaging conditions. Specifically, occurrence of similar regions (Atrophy) near disk boundary, irregular disk shape and boundary are the most essential aspects to be addressed by a OD segmentation method. A sample image is shown in Fig.2 to illustrate the above conditions. Detecting the cup boundary from a monocular image (without depth information) is a challenging task as depth is the *best* marker for cup. Medical experts use both appearance and anatomical knowledge to determine the cup boundary in different cup regions given only a monocular image. Anatomical evidence such as vessel bends at cup boundary is used as a reliable visual cue for determining cup boundary. Figure 1(b) shows the cup boundary marked by a glaucoma expert using such vessel bends (highlighted by arrows). The incorporation of

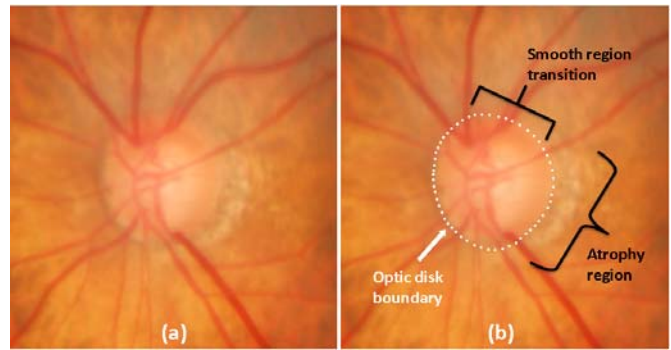


Fig. 2. a) Original color retinal image b) Highlighting ill-defined boundary region and image variation near OD boundary due to atrophy (a pathological change).

such knowledge for automated vertical cup-to-disk diameter ratio (CDR) estimation is seen in [19][20].

There are a few attempts at automated OD and cup segmentation from monocular images for structure segmentation as well glaucoma detection point of view [21][22][23][24][25][19]. It is noteworthy that works related to glaucoma detection focus *only* on the estimation of CDR which has been traditionally used to detect glaucomatous cases. However, CDR has been found to be inconsistent in explaining the amount of OD damage caused by glaucoma [26]. For instance, some patients have small CDR but significant visual field loss, whereas some have large CDR with little visual field loss. This is mainly argued to be due to limitations with the CDR parameter which cannot account for various configurations of optic cup and neuroretinal rim and focal notching (local enlargement of cup region). Consequently, an alternate OD evaluation methodology, called the *disc damage likelihood scale* has been introduced to precisely describe the amount of OD damage caused by glaucoma [26]. This is based on the appearance of the neuroretinal rim of the OD corrected for disc diameter.

Thus, an accurate segmentation of OD and cup is essential to get better localisation of neuroretinal rim to enable new glaucoma evaluation methodologies which consider other factors in addition to CDR. In this paper, we present a scheme for OD parameterisation which consists of two novel OD and cup segmentation methods. The aim is to derive a rich description of OD which is suitable for different glaucoma assessment methodologies. The proposed OD segmentation is robust to image variations with-in and near a OD region. The cup is modeled as a region enclosing pallor region (shown in fig. 1(a)) and defined by a boundary passing through a sparse set of vessel bends called relevant bends (*r-bends*). Results of a detailed evaluation of the proposed scheme on 33 normal and 105 glaucomatous images are also presented.

The organisation of the paper is as follows. Section II reviews related work on OD segmentation and describes the proposed method. In Section III existing approaches for cup segmentation from monocular CFI are reviewed and a new *r-bends* based cup segmentation method is presented. In Section IV the experiments and results are presented. We end with a discussion and conclusion in Section V.

## II. OD SEGMENTATION

### A. Background

Interest in OD segmentation is not limited to glaucoma detection. It is a fundamental task for automatic processing of retinal images such as image sequence registration, and automatic measurements for treatment evaluation or for diabetic retinopathy diagnosis [27]. Hence, there is a wider body of literature on OD segmentation which is briefly reviewed in this section.

Initial attempts have been made with shape-based template matching in which OD is modeled as a circular [28][29] [30] or elliptical [31] object. This matching is performed on an edge map extracted from the underlying image. This approach suffers due to vessel edges present in and around the OD region. To handle this, morphological-based pre-processing step is employed to suppress the vessel prior to template matching [30]. The circular template is further improved in [31] by considering intensity information inside and outside the OD region. The shape-based modeling of the disk region fails to characterise shape irregularity which typically arises due to some pathological changes or variation in view.

A number of gradient-based active contour models have been proposed to better capture shape irregularity in the disk region. In these approaches, a contour is initialised either manually [32] or automatically [33] and deformation in the contour takes place under the influence of energy term defined on the image gradient. The strategy is to first employ a gradient vector flow (GVF) based active contour model for disk boundary detection [34] followed by a minimisation of the effect on the perturbation in the energy value due to high gradient at vessel locations. This is achieved either by employing a pre-processing step [32] or by constraining the segmentation result to a circular or elliptically shaped object [35][36].

A variational, level-set based deformable model is proposed in which the obtained segmentation result is smoothed using an ellipse fitting operation [24]. While the enforcement of a shape model, either in the energy formulation or as a post-processing step, helps in handling local gradient minima it altogether limits the extraction range of irregular OD shapes which occur commonly in a clinical scenario. To overcome this limitation, a model-free snake approach which is an improvement over earlier active shape model [37][38], is proposed in [14]. In this approach, after each deformation, contour points are classified in a supervised manner into an edge-point cluster or uncertain-point cluster. The uncertain-point cluster mainly comprises of points which belong to the vessel region. The updating is only carried out on the contour points which belong to the edge-point cluster. Deformation of each point uses both global and local information to overcome local gradient variations. The successful results on both normal and challenging OD examples have been reported on which their earlier approach [37][38] was failing. This method shows promise in capturing a range of shape and image variations, however the accuracy in the segmentation is sensitive to the contour initialization.

More recently, work in active contours has been focused on region-based approaches[39] inspired by the basic idea

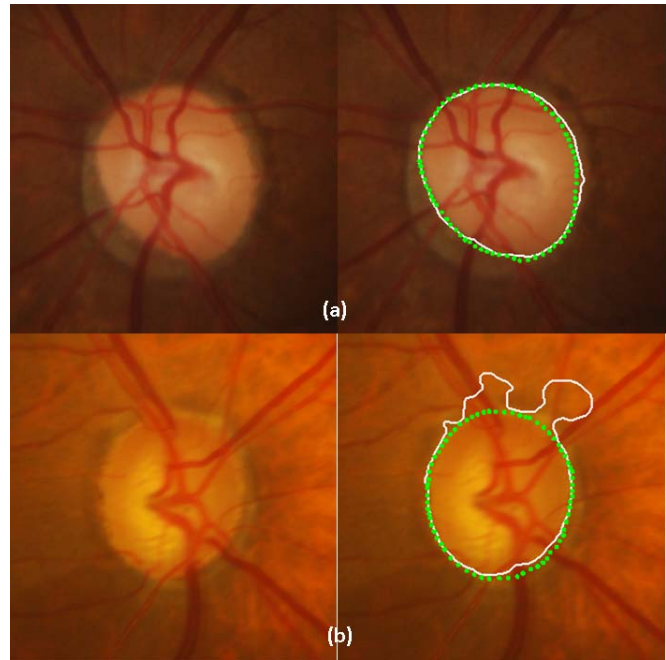


Fig. 3. Sample results of C-V active contour[39][41]. Green: Ground truth by an expert; White: Obtained result. a) First row: successful example, b) Second row: failure example.

of the Mumford-Shah model [40]. The advantages in using the region-based approaches over image gradient-based methods include the following: a) robustness against local gradient variations, b) feasibility of segmentation of color and multi-spectral images even in the absence of gradient-defined boundaries, c) lower sensitivity to contour initialisation and noise, and d) better ability to capture concavities of objects. In such models, foreground and background regions are modeled statistically and an energy functional is minimised to best separate foreground and background regions.

Figure 3(a) shows a successful segmentation on an image with large gradient distractions near boundaries [41]. However, in cases where the object to be segmented cannot be easily distinguished in terms of global statistics, region-based active contours may lead to erroneous segmentations. Figure 3(b) shows a failure example due to smooth region transition between object and background region. To handle such over-segmentation, traditional Chan-Vese (C-V) model has been modified by incorporating circularity constraint in [42]. However, restricting the scope of segmentation output to a certain shape, limits the extraction range of irregular OD shapes similar to the approaches described earlier.

Here, we propose a novel OD segmentation method based on region-based active contour model to improve the segmentation on the range of OD instances. The scope of the C-V model is enhanced by including image information at a support domain around each point of interest. The model is further refined to differentiate the OD region from the similar characteristic regions (atrophy) around it by integrating information from the multiple image feature channels. This method does not impose any shape constraint on the underlying model and hence is a good solution for OD segmentation. In the next

section, we explain the original C-V model and present our enhanced active contour model.

### B. Localised and vector-valued C-V active contour model

Consider a vector-valued function (image)  $I : \Omega \rightarrow \mathbb{R}^d$  where  $\Omega \subset \mathbb{R}^n$  is the image domain and  $d \geq 1$  is the dimension of the vector  $I(x)$ . In the problem at hand  $n=2$  and  $d=3$ . Let  $C(s) : [0, 1] \rightarrow \mathbb{R}^2$  be a piecewise parameterized  $C^1$  curve. For a gray valued image, the C-V model [39] defines an energy functional as:

$$E(c^+, c^-, C) = \lambda^+ \int_{inside(C)} |I(x) - c^+|^2 dx \quad (1) \\ + \lambda^- \int_{outside(C)} |I(x) - c^-|^2 dx \\ + \mu \text{length}(C)$$

where  $inside(C)$  and  $outside(C)$  represent the region inside and outside of the contour  $C$ , respectively and  $c^-$  and  $c^+$  are two constants that approximate the image intensity inside and outside of the contour. The parameters  $\lambda^+$ ,  $\lambda^- > 0$  and  $\mu > 0$  are weights for the fitting and the regularizing terms, respectively.

This model assumes that an image consists of statistically homogeneous regions and therefore lacks the ability to deal with objects having intensity inhomogeneity. Figure 3(b) shows an example. Intensity inhomogeneity is very common in natural images, especially in OD region it is a frequently occurring phenomena. In computer vision, there have been some attempts to improve C-V model for such situations [43] [44] [45]. Here, the basic idea is to use local instead of global image intensity into the region-based active contour model. These methods report significant improvement in the segmentation over original C-V model for segmenting objects with heterogeneous intensity statistics. However other than intensity heterogeneity within OD, smooth region transition at boundary locations and occurrence of similar characteristic regions near the OD boundaries (atrophy) make OD segmentation a much more difficult case altogether. Figure 8 illustrates more OD examples with additional challenges. The local intensity based statistics [43] [44] is not sufficient to discriminate between the OD and atrophy regions.

We propose a region-based active contour model which uses local image information at a support domain around each point of interest (POI) inspired by localised C-V models [43] [44] by using a richer form of local image information gathered over a multi-dimensional feature space. The intention is to represent the POI more holistically by including descriptions of the intensity, colour, texture, etc. This approach should yield a better representation of image regions and make the proposed model robust to the distractions found near the OD boundaries.

Let  $x$  and  $y$  denote two points in an image  $I$ . We define a local function  $\kappa$  for each  $x$  as:

$$\kappa(x, y) = \begin{cases} 1 & \text{if } \|x - y\| \leq r \\ 0 & \text{otherwise} \end{cases}$$

where,  $\kappa$  which defines the local image domain around a point  $x$  within a radius of  $r$ . Using the above function, the energy (mentioned in Eq.(1)) for a point  $x$  is redefined as:

$$E_x(h^+, h^-, C) = \lambda^+ \int_{\Omega_y} \kappa(x, y) |I(y) - h^+|^2 dy \quad (2) \\ + \lambda^- \int_{\Omega_y} \kappa(x, y) |I(y) - h^-|^2 dy$$

where,  $h^-$  and  $h^+$  are two constants that approximate region intensities inside and outside of the contour  $C$  respectively, near the point  $x$ . The local function ensures the value of  $h$  that minimises  $E_x(h^+, h^-, C)$  is only influenced by the image information within the local domain. This way the behavior of any individual point is constrained by the regional information from a local domain. This helps in capturing local boundaries which get missed by a C-V model due to small difference in the global statistics of interior and exterior region of the contour.

Now, we incorporate information from a multi-dimensional feature space, in the above model. Let  $I_i$  be the  $i^{th}$  feature of an image on  $\Omega$  with  $i=1, \dots, d$ . The extension of the above model to the vector case is:

$$\bar{E}_x(h^+, h^-, C) = \frac{1}{d} \sum_{i=1}^d \lambda_i^+ \int_{\Omega_y} \kappa(x, y) |I_i(y) - h_i^+|^2 dy \quad (3) \\ + \frac{1}{d} \sum_{i=1}^d \lambda_i^- \int_{\Omega_y} \kappa(x, y) |I_i(y) - h_i^-|^2 dy$$

where  $h^+ = (h_1^+, \dots, h_d^+)$  and  $h^- = (h_1^-, \dots, h_d^-)$  are two constant vectors approximating regions' feature values inside and outside the contour  $C$  respectively in each feature space. The  $\lambda_i^+ > 0$  and  $\lambda_i^- > 0$  are weight parameters for the error term defined for each feature space.

The above energy  $\bar{E}_x$  defined for a point  $x \in \Omega$  can be minimised when this point is exactly on the object boundary and values of  $h^+$  and  $h^-$  are optimally chosen. The integral of  $\bar{E}_x$  over all points  $x$  is minimised to obtain the entire object boundary. This is defined as:

$$E(h^+, h^-, C) = \int_{\Omega} \bar{E}_x(h^+, h^-, C) dx \quad (4)$$

This energy is converted to an equivalent level-set formulation [46] for curve evolution.

1) *Level-set formulation of the model:* In a level-set formulation, a contour  $C \subset \Omega$  is represented by the zero level set of Lipschitz function  $\phi : \Omega \rightarrow \mathbb{R}$ . In this representation, the energy functional  $\bar{E}_x(h^+, h^-, C)$  in (3) can be rewritten as

$$\bar{E}_x(h^+, h^-, \phi) = \frac{1}{d} \sum_{i=1}^d \lambda_i^+ \int_{\Omega_y} \kappa(x, y) |I_i(y) - h_i^+|^2 H(\phi(y)) dy \quad (5) \\ + \frac{1}{d} \sum_{i=1}^d \lambda_i^- \int_{\Omega_y} \kappa(x, y) |I_i(y) - h_i^-|^2 (1 - H(\phi(y))) dy$$

where  $H$  is the Heaviside function. Now, the energy term in (4) can be written as:

$$\begin{aligned}
E(h^+, h^-, \phi) &= \int_{\Omega} \bar{E}_x(h^+, h^-, \phi) \quad (6) \\
&= \int_{\Omega} \left[ \frac{1}{d} \sum_{i=1}^d \lambda_i^+ \int_{\Omega_y} \kappa(x, y) |I_i(y) - h_i^+|^2 H(\phi(y)) dy \right] dx \\
&+ \int_{\Omega} \left[ \frac{1}{d} \sum_{i=1}^d \lambda_i^- \int_{\Omega_y} \kappa(x, y) |I_i(y) - h_i^-|^2 (1 - H(\phi(y))) dy \right] dx
\end{aligned}$$

A distance regularization term [44] is incorporated to penalise the deviation of  $\phi$  from a signed distance function characterised by the following integral:

$$\xi(\phi) = \int_{\Omega} \frac{1}{2} (|\nabla \phi(x)| - 1)^2 dx \quad (7)$$

To regularise the zero level contour of  $\phi$ , the length of zero level curve of  $\phi$  is also added which is given as:

$$\zeta(\phi) = \int_{\Omega} \delta \phi(x) |\nabla \phi(x)| dx \quad (8)$$

Now, we define the entire energy functional as

$$F(h^+, h^-, \phi) = E(h^+, h^-, \phi) + \alpha \xi(\phi) + \beta \zeta(\phi); \quad (9)$$

where  $\alpha$  and  $\beta$  are non-negative constants. This energy functional is minimised to the OD boundary. The minimisation method and performed approximations are provided in the appendix.

### C. OD localisation and contour intialisation

The first step is to localise the OD region and extract a region of interest for further processing. The red colour plane of CFI gives good definition of OD region and thus is a good choice for the OD localisation task. The contour initialisation is the next essential step to initiate the active contour evolution. In our method, we perform localisation and initialisation steps together by performing circular Hough transform [47] on the gradient map.

The vessel segments are identified using a curvature-based technique [48]. These regions are suppressed and inpainted by performing selective morphological closing in 8 directions and retaining maximum response for each vessel pixel. Next, a Canny edge detector at a very low threshold is applied on the pre-processed (vessel-free) image to get edge points. On these points, a circular Hough transform is applied for a range of expected OD radius ( $r_{min}$  to  $r_{max}$ ). This range is chosen based on the retinal image resolution.

We select the OD center which has maximum value in the accumulator matrix while performing Circular Hough transform. Next, the edges near the identified center location in the image domain are used to estimate the radius of the circle. The circle points are identified using estimated radius and used to initialise the active contour mentioned in section II-B.

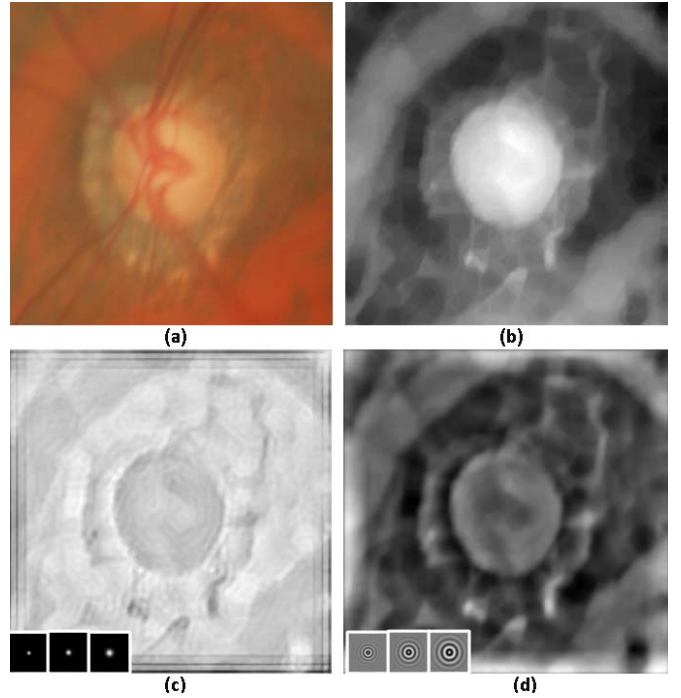


Fig. 4. Different feature space representation for the OD region. a) Original colour image, b) Red colour plane, c) Texture space-1, and d) Texture space-2.

### D. Segmentation in multi-dimensional feature space

A multi-dimensional image representation is obtained from colour and texture feature space. In normal image conditions, red colour plane gives a better contrast of the OD region. To better characterise OD in pathological situations, two different texture representations are derived.

First, Gaussian filter responses obtained at three fine scales  $\sigma = \sqrt{2}, 2, 2\sqrt{2}$  are integrated together by summing. Second, we use a special class of texture filter bank proposed in [49] defined as:

$$L(c, \sigma, \tau) = L_0(\sigma, \tau) + \cos\left(\frac{\pi\tau c}{\sigma}\right) e^{-\left(\frac{c^2}{2\sigma^2}\right)}$$

where  $\tau$  is the number of cycles of the harmonic function within the Gaussian envelope of the filter, commonly used in the context of Gabor filters.  $L_0(\sigma, \tau)$  is added to obtain a zero DC component. These filter responses are obtained at three pairs  $(\sigma, \tau) = (4, 2), (6, 3), (8, 3)$  and summed together to capture regularity in the texture profile at a finer level. These responses are computed on the red colour plane of the image. Prior to this computation, the points belonging to the vessel region are removed and interpolated as mentioned in section II-C. In general, the choice of texture representation is driven by the discriminability it provides to help distinguish OD region from the various atrophy regions occurring near to the OD. Figure 4 shows three different feature space representations.

Now, an image point  $x$  is represented by a three element vector where value of individual vector element is taken from red colour plane, texture feature space 1 & 2, respectively. This vector-valued image is used by the active contour model presented in section II-B to get the OD boundary.

### III. CUP SEGMENTATION

#### A. Background

Very few methods have been proposed for cup segmentation from monocular image. Since 3-D (depth) images are not easily available, Liu et. al. [25] proposed a method in which a potential set of pixels belonging to cup region is first derived based on the reference colour obtained from a manually selected point. Next, an ellipse is fit to this set of pixels to estimate the cup boundary. A variant of this method obtains the cup pixels via thresholding of the green colour plane [25]. Cup boundary obtained via ellipse fitting yields only coarse cup boundary. In [41], cup symmetry is used after thresholding to obtain a coarse cup segmentation. However, fixed thresholding is also not adequate to handle large intensity variations in the cup region that arise due to physiological difference across patients. The energy minimization-based deformable models are not appropriate for this problem due to the absence of edge or region based information associated with the cup region to derive an energy functional.

In order to address these problems, additional information such as small vessel bends ('kinks') which anatomically mark the cup boundary have been used in [19]. The bends of small vessels as they traverse from the disc to the cup, provide a physiological validation for the cup boundary [19][20]. In [19], image patches are extracted around an estimated cup boundary obtained in [25] and vessel pixels are identified using edge and wavelet transform information. Next, vessel bends, characterized by points of direction change in the vessel pixels are detected and used to obtain the cup boundary. This method is highly dependent on the preliminary cup boundary obtained from [25]. Furthermore, the statistical rule for selecting vessel pixels is very sensitive to the inter-image variations.

Typically, both appearance and anatomical knowledge are considered by the glaucoma experts to determine cup region. Hence, we propose a method that integrates both these information under a common framework. The cup is modeled as a region enclosing the pallor region (shown in fig. 1(a)) and defined by a boundary passing through a sparse set of vessel bends.

#### B. Cup segmentation using $r$ -bends information

The objective is to segment the cup region by using both vessel bends and pallor information. As seen in fig. 1(b) and cyan points in fig. 6(b), vessel bends can occur at many places within the OD region. However, only a subset of these points define the cup boundary. We refer to this as relevant vessel bends or  $r$ -bends. The first problem at hand is to find this subset. We use multiple sources of information for this purpose: the pallor region which spatially defines the inner limit of  $r$ -bends, bending angle and location in the OD region. A second problem is that the anatomy of the OD region is such that the  $r$ -bends are non-uniformly distributed across a cup boundary with more points on the top and bottom; they are mostly absent in the nasal side and very few in number in the temporal side. We propose a local interpolating spline to naturally approximate the cup boundary in regions where  $r$ -

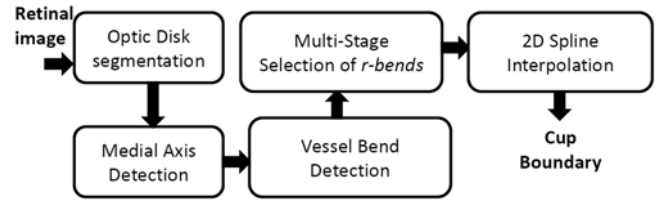


Fig. 5. The proposed cup segmentation method

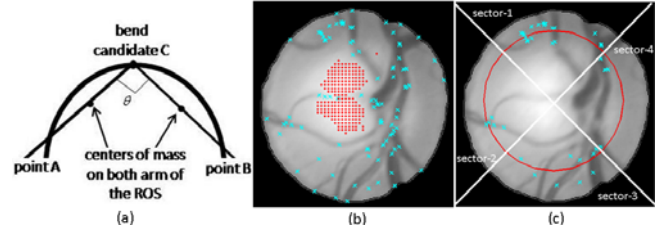


Fig. 6. a) Angle of a vessel bend, b) uniform pallor samples (red), bend points (cyan) and c) fitted circle (red) and potential  $r$ -bends

$r$ -bends are absent. Figure 5 shows an overview of the proposed method.

1) *Medial axis detection*: The OD region has both thick and thin vessels. Detecting both reliably is difficult in the presence of inter-image intensity variations. Several methods have been proposed for vessel segmentation in literature (see [50]). We follow a method proposed earlier by us [48] which formulates the blood vessel detection as a problem of trench detection in the intensity surface. The selection of this space gives robustness to the image variations and detection is solely driven by the shape of trench and directional continuity associated with a vessel structure. Trenches are regions characterized by high curvature, oriented in a particular direction.

The curvature is computed using surface tangent derivative [48] defined as:

$$\Upsilon(x) = \frac{d^2y/dx^2}{1 + (dy/dx)^2}$$

For each point,  $\Upsilon$  is computed in 4 different directions. The maximum value of the responses  $\Upsilon_{max}$  and corresponding orientation  $\alpha$  (perpendicular to the vessel direction) are retained and further assessed to obtain trench points. A point is declared as a trench if value of  $\Upsilon_{max}$  is greater than both threshold value  $t$  and the values of neighboring pixels in  $\alpha$  direction.

For the robust detection of low contrast vessels, we employ a two-phase thresholding scheme in which first, a high value of  $t$  is applied to get high contrast vessel points (set-1). Then, low value of  $t$  is applied to get a new set of low contrast vessel points (set-2). Points in set-2 which are found connected to the set-1 are included in the final set along with set-1. This strategy helps in successfully extracting low contrast vessels while rejecting noise. The final trench points give a medial axis-based representation of vessel structure which is more precise in quantifying vessel bends compared to edge-based representation. The next task is to extract vessel bends from this representation.

**Algorithm 1** Multi-Stage selection of  $r$ -bends

- 1: **Coarse Selection:** Fit a circle to the set of candidate bends  $b_i$  and bright pixels in the pallor region
- 2: Select the bends which lie in the vicinity of this circle for the next stage
- 3: **Fine Selection:** Classify the bends into two categories: a) sector 1&3, b) sector 2&4
- 4: Compute the parent vessel-segment orientation  $b_i^\theta$  for each bend  $b_i$
- 5: Scan each sector in steps of  $20^\circ$
- 6: **if** Bend(s) exist **then**
- 7:   **if**  $b_i^\theta$  is correct **then**
- 8:     **if** multiple **then**
- 9:       Select  $r$ -bend with least bend angle
- 10:    **else**
- 11:     Select  $r$ -bend
- 12:    **end if**
- 13: **end if**
- 14: **else**
- 15:   continue
- 16: **end if**

2) *Vessel Bend detection:* The amount of bending in vessels varies according to the caliber of vessel. Thin vessels show significant bending compared to a thick vessel. This is due to the fact that thick vessels are more rigid. The selection of appropriate scale for detecting bends in both types of vessels is crucial because bend in a thick vessel is apparent only at a larger scale compared to a bend in thin vessel. We employ a scheme based on the concept of dynamic region of support (ROS) which has been proposed for corner detection [51] to find the appropriate scale to analyse a candidate point. This is explained below.

First, we extract vessel segments terminated by end and/or junction points. For each segment, we compute 1D shape (curvature) profile and locate the local maxima. These local maxima constitute a candidate set of bends  $b_i$ . A ROS for any  $b_i$  is defined as a segment of vessel around  $b_i$  and bound on either side by the nearest curvature minimum. Choosing the bounds to be based on curvature minima automatically ensures the size of the ROS to be large for thick vessels and small for thin vessels. The angle of bend  $\theta$  is then computed as the angle between the lines joining a bend point and the centers of mass on both sides of the ROS. The center of mass of an arm is defined by the mean position of pixels on the arm (illustrated in fig. 6(a)). Since only vessels bending into the cup are of interest, bends above  $\theta = 170^\circ$  are eliminated from the candidate set. The detected vessel bends in a sample image are highlighted in fig. 6(b) with cyan markers.

3) *Multi-stage selection of  $r$ -bends:* The task of identifying the  $r$ -bends from  $b_i$  is performed in two stages to reduce the required analysis, by utilizing anatomical knowledge associated with  $r$ -bends. In the first stage, a coarse selection is done based on a bend's proximity to the pallor region. In the second stage, the spatial position and bending information are used to identify the set of  $r$ -bends.

*Coarse Selection:* Let  $p : (x_p, y_p)$  be a set of points within

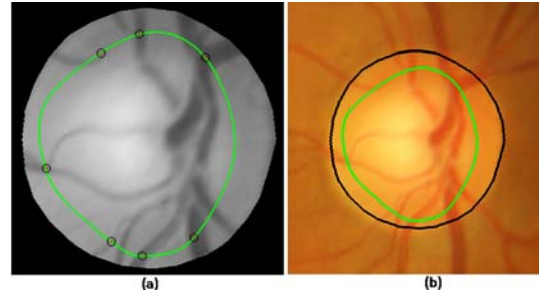


Fig. 7. a) Estimated cup boundary, b) final OD and cup boundary.

the pallor region. These are found by retaining the top 25% of the bright pixels within the OD. Next, let  $b : (x_b, y_b)$  be the locations of the bends  $b_i$ . The region containing potential  $r$ -bends is localised by finding a best-fit circle (in the least-squares sense) to the set of points  $(x, y) = \{p, b\}$ . The bends which lie in the vicinity of this circle (inside and outside) are passed to the next stage. Figure 6(c) shows sample candidate  $r$ -bends obtained in this stage.

*Fine Selection:* Each candidate bend is analysed in terms of its sector-wise location (as in fig. 6(c)) and its parent vessel orientation. This analysis is based on anatomical knowledge that bends formed by vertical vessels in Sec-1&3 and horizontal vessels in Sec-2&4 are the probable  $r$ -bends. The final refined set of  $r$ -bends is found as follows: A sector is radially analysed with a step size of  $20^\circ$  and in each step, only bends formed by vessels with the 'correct' orientation are retained. If multiple bends remain, then the bend with smaller value of  $\theta$  is selected as thin, rather than thick, vessel bends are more reliable indicators for the cup boundary. These usually occur in the diagonal region between two sectors. The complete selection procedure is also illustrated in Algo. 1.

4) *2D spline interpolation:* Typically,  $r$ -bends are sparse and not uniformly distributed across the sectors. In their absence, experts use their clinical knowledge (experience of direct 3D cup examination) to approximate a cup boundary. Hence, it is difficult to get the cup boundary in the regions with no  $r$ -bends. We choose a *local*, cubic cardinal spline, which is a generalisation of Catmull-Rom spline, with a shape parameter  $t$ . The parameter  $t$  helps control the bending behaviour and thus the shape according to the sector. The value of  $t$  is kept high in sectors 2&4 as they usually have low vessel density ( $r$ -bends) compared to sector 1&3. A closed-form 2D spline curve is obtained by considering, sequentially a subset of  $r$ -bends. Figure 7(a) shows the interpolated cup boundary passing through the  $r$ -bends and Fig. 7(b) shows final obtained boundaries for a sample OD region.

## IV. EXPERIMENT AND RESULTS

### A. Dataset

The proposed method was tested on a dataset of retinal images collected from an ongoing pilot study in collaboration with a local eye hospital. The dataset has 33 normal and 105 glaucomatous (total of 138) images. All images were taken under a fixed protocol with 30-degree field of view, centered on the OD and of dimension  $2896 \times 1944$  pixels. For

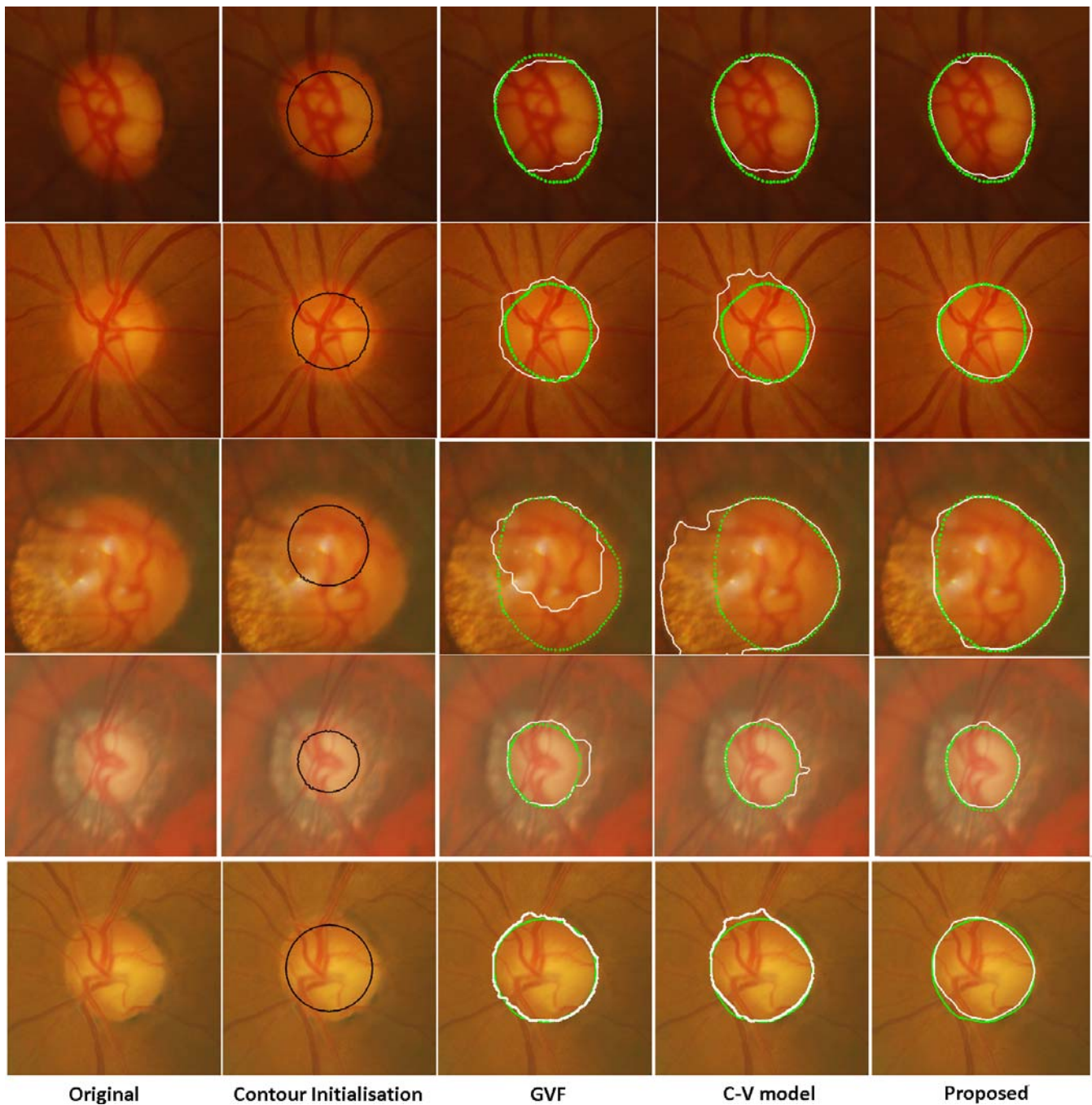


Fig. 8. OD segmentation results. First column: original image; Second column: initialised contour; Third column: GVF results; Fourth column: C-V model results; Fifth column: proposed method results. Green colour indicates boundary marked by an expert and white colour indicates obtained boundary by a method. The last two rows show representative examples of high atrophy condition.

each image, ground truth was collected from three glaucoma experts, referred to as Expert-1, Expert-2 and Expert-3 with experience of 3, 5 and 20 years, respectively. To compensate for inter-observer marking variations, we also derived an average OD boundary for each image by averaging boundaries obtained from three experts. This average boundary will be referred to as *Expert-A*. The evaluation of the algorithm has been carried out against three experts individually and also against average expert marking.

### B. Evaluation Measures

For OD segmentation, different comparisons have also been made with two known active contour models: a) gradient vector flow (GVF) [32], and b) C-V model [41]. In order to assess the strength of individual active contour models, curve initialisation and pre-processing are kept same for each model. Similarly, for cup segmentation, the performance of the proposed method is compared against two commonly used approaches: a) Thresholding [41], and b) Ellipse fitting [25].

A common quantitative analysis is performed to assess over-

all performance of both OD and cup segmentation methods. This evaluation is based on the similarity in the a) detected area and in the b) detected boundary against each individual expert and average expert marking.

To assess the area overlap between computed region and ground truth, the pixel-wise precision and recall values are computed. These are defined as:

$$Precision = \frac{tp}{tp + fp} \quad Recall = \frac{tp}{tp + fn}$$

where  $tp$  is the number of true positive,  $fp$  is the number of false positive and  $fn$  is the number of false negative pixels. To better appreciate results, we compute a single performance measure called traditional F-score (F) that is the harmonic mean of precision and recall. It is defined as:

$$F = 2 \frac{Precision \cdot Recall}{Precision + Recall}$$

This is also known as the  $F_1$  score, because recall and precision are evenly weighted. The value of F-score lies between 0-1 and for an accurate method, F-score value should be high.

A boundary-based evaluation was done by measuring the distance between two closed boundary curves. This helps assess the accuracy of boundary localisation. Let  $C_g$  be the boundary curve marked by the expert and  $C_o$  be the curve obtained by a method. The distance (D) between two curves is defined as (in pixels):

$$D = \frac{1}{n} \sum_{\theta=1}^{\theta_n} \sqrt{(d_g^\theta)^2 - (d_o^\theta)^2}$$

where,  $d_g^\theta$  and  $d_o^\theta$  are the distance from centroid of curve  $C_g$  to points on  $C_g$  and  $C_o$ , respectively in the direction of  $\theta$  and  $n$  is the total number of angular samples. The distance between the computed boundary and ground truth should ideally be close to zero.

The area and contour information were also used to compute two standard disk parameters used in glaucoma detection. These are the ratio of cup-disk: a) vertical diameters and areas. This was computed for the proposed system and compared against three experts and average expert marking.

### C. Results

1) *OD segmentation*: Figure 8 shows sample test images and results obtained by three different active contour models (in the last three columns). The radius  $r$  defined for the function  $\kappa$  is fixed at 40 pixels for all the reported experiments. The second column illustrates the initialised contour obtained by the scheme mentioned in section II-C. The first row presents an example of an irregularly shaped OD with high gradient variations near the initialised contour. The GVF model fails to capture the entire OD region due to local gradient minima. The C-V model is able to handle local gradient variations however low bright regions get excluded due to a subtle difference present between average intensity of the detected foreground and background regions. The proposed method performs better and captures the boundary except where the boundary regions are occluded by thick blood vessels. This situation mainly

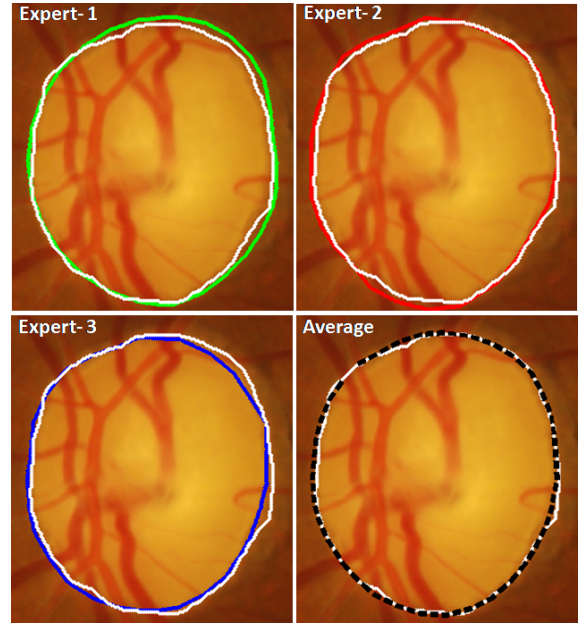


Fig. 9. Evaluation against three experts and expert-A. White contour: computed result; other colours: expert marking.

arises due to the pre-processing carried out to suppress the vessel pixels. The vessel pixels at the boundary are usually get interpolated by the background pixels (outside OD region) therefore considered background by the proposed method. The second row presents an example of fuzzy OD boundary where the proposed method better captures the OD boundary compared to other methods. The third and fourth rows show two successful segmentation results on two challenging and high atrophy cases. The fifth row shows an example where GVF result has better overlap with localisation compared to other two models. This is mainly due to the gradient information in some regions being a stronger cue than multi-features. However, it can be seen that information integration over multiple feature plane helps in obtaining smooth OD boundary.

Next, we present a detailed look at one of the results (in Figure 9) to illustrate the inter-observer variability (subjectivity) present in the expert marking and the need for deriving an average boundary (Expert-A). This example has a good definition of OD boundary and it is carefully selected to demonstrate subjectivity, a well known aspect in medical image analysis on a well defined case. This subjectivity is mainly due to an expert's level of clinical experience and partly due to their comfort level with the marking tool. The obtained contour by the proposed method has better consensus with the average marking compared to individual expert markings.

In order to assess the overall performance on the dataset, the computed average F-score and boundary distance figures are given in Table I-A. From this table, it can be observed that the proposed method has the highest performance as it has the highest F-score and minimum distance between derived boundary and the averaged boundary. This table presents the overall performance and does not illustrate the difference in performance on difficult cases. The differential performance on

TABLE I  
A) AVERAGE F-SCORE, AND B) AVERAGE BOUNDARY DISTANCE COMPUTED IN RADIAL DIRECTION ON THE ENTIRE DATASET.

	A: F-Score						B: Boundary Distance (in pixels)					
	OD Segmentation			Cup Segmentation			OD Segmentation			Cup Segmentation		
	GVF	CV model	Ours	Threshold	Ellipse Fitting	r-bends	GVF	CV model	Ours	Threshold	Ellipse Fitting	r-bends
<b>Expert-1</b>	0.90	0.95	0.96	0.66	0.67	0.80	33.2	14.8	12.9	45.5	44.6	27.7
<b>Expert-2</b>	0.88	0.94	0.95	0.65	0.67	0.83	35.3	15.6	14.2	48.1	46.0	24.7
<b>Expert-3</b>	0.91	0.96	0.97	0.71	0.72	0.81	30.1	13.5	10.8	36.1	35.2	24.9
<b>Expert-A</b>	0.90	0.96	<u>0.97</u>	0.68	0.69	<u>0.84</u>	31.2	13.1	<u>11.1</u>	42.4	40.6	<u>23.2</u>

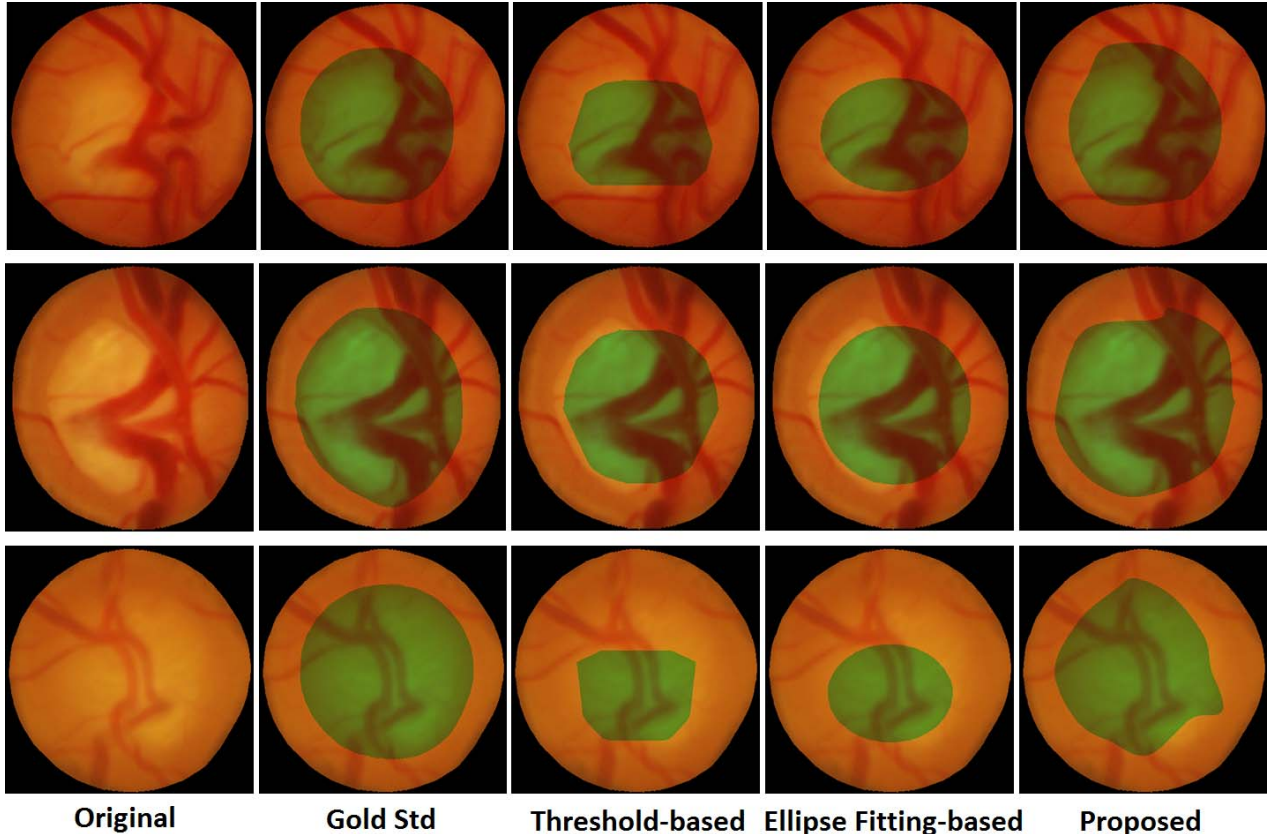


Fig. 10. Cup Segmentation Results. First column: original image; Second column: Expert-A; Third column: Threshold-based method [41]; Fourth column: ellipse Fitting-based [25]; Fifth column: proposed method results.

a subset of 8 difficult images (see Fig. 11 for sample images) having slowly varying OD boundaries or atrophy regions is reported in Table II. The figures here clearly reflect the limitations of C-V model. The GVF performs is able to avoid over segmentation due to its sensitivity to the small gradient changes. To examine the over/under segmentation of these 3 methods, we computed the average *signed* boundary distance on these 8 difficult images (refer to Table III). The positive values obtained by GVF model indicate under-segmentation results whereas C-V model gives over-segmentation results. Hence, based on these evaluations, we conclude that the presented model achieves better and *consistent* segmentation compared to the GVF and C-V models.

The selection of radius parameter  $r$ , which defines the local image domain around a point of interest, is important. For

example, a small radius will increase the model's sensitivity to small gradients within the local image domain and lead to a behaviour similar to GVF model. Whereas, a large  $r$  will decrease the sensitivity to small gradients and result in the model behaving similar to the C-V model. Based on the high image resolution and typical scale of OD boundaries in the dataset,  $r = 40$  was found to give the best performance. Next, we present the cup segmentation results.

2) *Cup segmentation*: Sample test images and results obtained with the proposed r-bend based scheme are shown in Fig. 10. For comparison, the segmentation results obtained by two other methods: i) thresholding-based and ii) ellipse fitting-based, are also shown. Overall, the proposed characterisation for the cup region establishes its potential with a significant improvement in the segmentation results when compared to

TABLE II  
A) AVERAGE F-SCORE, AND B) AVERAGE BOUNDARY DISTANCE  
COMPUTED IN RADIAL DIRECTION ON 8 DIFFICULT IMAGES.

	A: F-Score			B: Boundary Distance (in pixels)		
	GVF	CV model	Ours	GVF	CV model	Ours
Expert-1	0.91	0.76	0.93	14.99	42.13	12.30
Expert-2	0.91	0.78	0.94	16.18	39.13	11.43
Expert-3	0.92	0.76	0.93	13.37	40.17	12.02
Expert-A	0.91	0.78	<u>0.94</u>	14.84	39.43	<u>11.92</u>

TABLE III  
AVERAGE SIGNED BOUNDARY DISTANCE ( $d_g^g - d_o^g$ ) ON 8 DIFFICULT  
IMAGES.

	GVF		C-V model		Ours	
	mean	std	mean	std	mean	std
Expert-1	7.38	10.14	-19.85	25.70	-2.02	12.90
Expert-2	11.61	8.86	-18.19	22.72	2.34	11.32
Expert-3	5.26	8.62	-21.66	25.22	-4.08	12.35
Expert-A	8.77	8.78	-19.30	26.00	<u>-0.44</u>	<u>12.09</u>

the other two methods.

A closer look at the results reveals that the segmentation accuracy is higher at the detected *r-bends* than in locations which do not have vessel bends. This can be more clearly seen in the last row. Here, better segmentation is achieved in the dense vessel region (the left/nasal side) compared to the right/temporal side. To explain this further, we show the detected cup boundary against three experts on a sample image (overlaid on segmented OD region) in Fig. 12. It can be seen that the cup boundary at *r-bends* is closer to the expert marked boundaries (fig. 12(a-2)), whereas in regions where they are absent, the interpolated result is unable to match the boundary marked by the experts. However, a fair degree of disagreement between experts at *no bend region* attests to the complexity of the problem. We also observed some challenging situations where our detected *r-bends* are not considered relevant by experts. For instance, in fig. 12(a-1) boundaries marked by experts are away from the detected *r-bends* though there was no 2D clue present to support their markings.

Table I-B presents the quantitative assessment of the cup

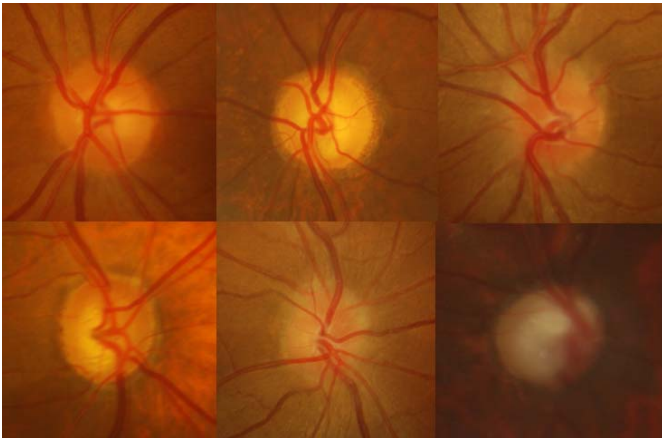


Fig. 11. Sample difficult images.

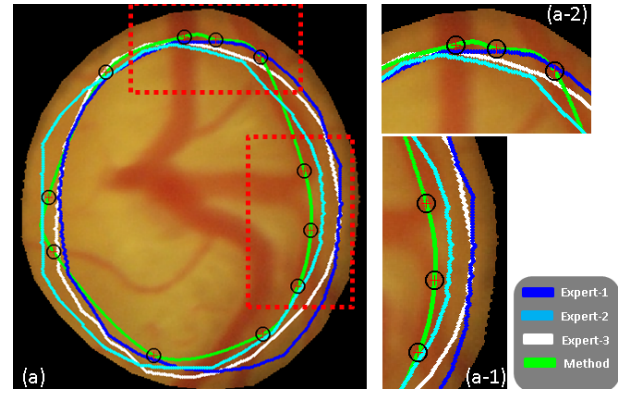


Fig. 12. Detected cup boundary.

segmentation results using F-score and distance of derived boundary to ground truth. The obtained results shows that proposed method gives significant improvement in performance in both F-score and boundary-based measures compared to other two methods. Overall, the proposed cup segmentation method performs well against expert-A. This improvement in the performance justifies the role of proposed characterisation for the cup.

3) *Parameter estimation for glaucoma assessment*: Glaucoma assessment is based on the cup disk diameter ratio (CDR), with the diameter measured in the vertical direction. We assess our proposed system by computing this parameter and one other parameter which is the ratio of cup and disk *areas*. The area ratio is selected to assess the overall segmentation accuracy achieved in all directions unlike the CDR which reflects accuracy only in vertical direction. Accuracy in estimating area ratio parameter indicates suitability of the proposed segmentation methods in deriving other disk parameters. For instance, an alternate glaucoma assessment scheme [26] takes into account of the neuroretinal rim region to quantify the focal cupping. This requires an accurately segmented disk and cup.

Both CDR and area ratios are computed and assessed against ground truth which comprises of three experts and their average marking. Figure 13 shows parameter values obtained from the ground truth and from the proposed system on a sample image. The estimated value of the CDR is considerably good notwithstanding the disagreement between experts. Whereas, the obtained value of area ratio indicates a case of cup over-segmentation. For an overall assessment, the mean  $\mu$  and standard deviation  $\sigma$  of the error in estimating both parameters for 33 normal and 105 glaucomatous images are computed and reported in Table. IV. The figures indicate that the average estimation error  $\mu, \sigma$  for both parameters is much smaller in glaucomatous images compared to normal images over all four ground truths. This indicates high sensitivity in glaucoma detection by the proposed method. For comparison, we consider the inter-observer variability. The CDR estimation error for expert-2 against expert-1, taken as ground truth, yields the following results: the mean/standard deviation of error for CDR are 0.10/0.08 for normal case and 0.08/0.05 for glaucoma case. The corresponding figures for

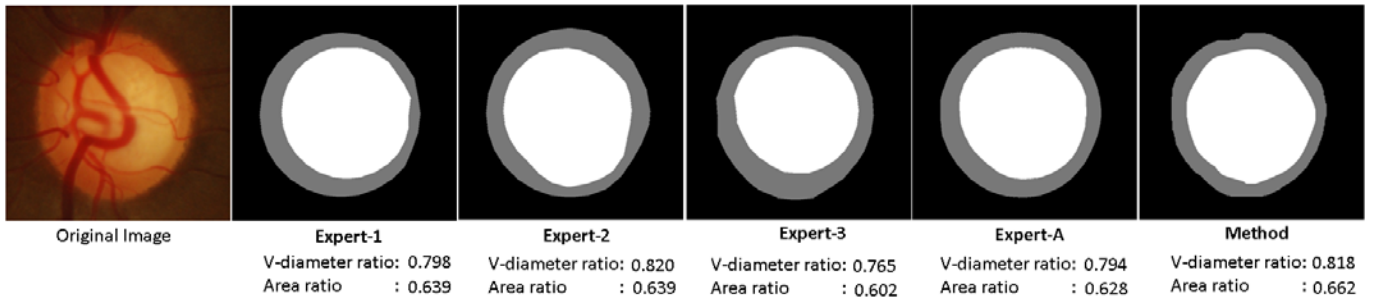


Fig. 13. Estimated CDR against ground truth.

TABLE IV  
ESTIMATION ERROR IN A) CUP-TO-DISK AREA AND B) VERTICAL DIAMETER RATIO

Category/No.	A: Cup-to-Disk Vertical Diameter Ratio								B: Cup-to-Disk Area Ratio							
	Expert-1		Expert-2		Expert-3		Expert-A		Expert-1		Expert-2		Expert-3		Expert-A	
	$\mu$	$\sigma$	$\mu$	$\sigma$	$\mu$	$\sigma$	$\mu$	$\sigma$	$\mu$	$\sigma$	$\mu$	$\sigma$	$\mu$	$\sigma$	$\mu$	$\sigma$
<b>Normal/33</b>	0.26	0.15	0.18	0.11	0.21	0.11	0.21	0.13	0.33	0.20	0.25	0.15	0.29	0.17	0.28	0.17
<b>Glaucoma/105</b>	0.09	0.08	0.10	0.08	0.09	0.08	0.09	0.08	0.12	0.10	0.12	0.10	0.12	0.11	0.10	0.09
<b>Total/138</b>	0.13	0.13	0.12	0.09	0.12	0.10	0.12	0.11	0.17	0.16	0.15	0.13	0.16	0.14	0.15	0.14

the area ratio are as follows: 0.11/0.10 for normal case and 0.11/0.08 for glaucoma case. These results indicate that the sensitivity of proposed method in estimating both parameters on glaucomatous images is within the range of inter-observer variability found between experts.

To sum up, we have presented qualitative and quantitative results of assessment of the proposed segmentation methods which includes a comparison against some standard existing schemes. There are a few insights which can be drawn from our experiment results. With respect to the glaucoma assessment via CDR or areas ratio, the proposed method is more accurate in estimating CDR as it yields a smaller average error against three experts and their average, as seen from the last row of the Table IV. This indicates higher segmentation accuracy in vertical direction for both OD and cup. The source of higher error in the estimation of area ratio is due to the inaccuracy of cup segmentation method particularly in nasal and temporal side where no 2D clue such as *r-bends* are found. In such regions, due to the loss of depth information in monocular images, a good degree of disagreement can also be seen between experts as explained in Section IV-C2. Moreover, the tendency for disagreement between experts was found to be more in the case of normal rather than glaucomatous images. It is noteworthy that the error in the estimation of CDR and area ratio is consistently small and similar across experts for glaucomatous images which indicates high consensus between experts in OD and cup boundaries compared to normal images.

## V. CONCLUSION

In this paper, we presented a solution for glaucoma assessment which allows derivation of various geometric parameters of the OD. This is in contrast to earlier approaches which have largely focused on the estimation of CDR which varies considerably within normals. It is also well recognised that there is significant intra and inter observer error in manual

assessment with this parameter [26]. Alternative OD parameters have been considered important to indicate glaucomatous progression and staging based on the configurations of optic cup and neuroretinal rim [26] etc. The presented work enables more comprehensive evaluation of the OD and performing glaucoma detection using multiple disk parameters.

The presented solution for glaucoma assessment was in the form of two segmentation methods for OD and cup. A novel, active contour model is presented to get robust OD segmentation. This has been achieved by enhancing the C-V model by including image information at the support domain around each contour point. An attractive aspect of the extension is the strengthening of region-based active contour model by the integration of information from multiple image feature channels. The obtained results show that our method captures OD boundary in a unified manner for both normal and challenging cases without imposing any shape constraint on the segmentation result, unlike the earlier methods. Since the proposed enhancement of the C-V model is general, its scope is not limited to OD boundary detection but is widely applicable to other segmentation applications, especially in the medical imaging domain. However, this model is computationally more intensive (depending on the value of  $r$ ) than the C-V model since local image statistics over multiple feature planes is utilised. A novel cup segmentation method using *r-bends* information is also presented. Trench-based vessel modeling and a region of support-based bend detection that have been employed to build robustness to varying thickness of the vessels. The final cup boundary is obtained using local spline interpolation on the detected *r-bends*.

In summary, both segmentation methods have been extensively evaluated on a dataset of size 138 images, with associated ground truth from 3 experts and compared against existing approaches. In cup segmentation, it is observed that boundary estimation errors are mostly in regions with no

depth cues which is consistent with the high inter-observer variability in these regions. This signals the ambiguity in 2D information and the importance of 3D information in cup segmentation which will be investigated in our future work. Overall, the obtained results of the proposed method for glaucoma assessment, via OD parametrisation, establishes the potential for an effective solution for glaucoma screening.

#### APPENDIX A

The Heaviside function  $H$  in Eq. (5) is approximated by a smooth function  $H_\varepsilon$  defined by

$$H_\varepsilon(x) = \frac{1}{2} \left[ 1 + \frac{2}{\pi} \arctan \left( \frac{x}{\varepsilon} \right) \right] \quad (10)$$

The derivative of  $H_\varepsilon$  is the following smooth function

$$\delta_\varepsilon(x) = H'_\varepsilon(x) = \frac{1}{\pi} \frac{\varepsilon}{\varepsilon^2 + x^2} \quad (11)$$

The approximation of  $H$ ,  $\delta$  by  $H_\varepsilon$ ,  $\delta_\varepsilon$  respectively, in Eq. (5) and Eq. (8) gives an approximated form of energy functional given in Eq. (9).

$$F_\varepsilon(h^+, h^-, \phi) = E_\varepsilon(h^+, h^-, \phi) + \alpha \xi(\phi) + \beta \zeta_\varepsilon(\phi); \quad (12)$$

The value for  $\varepsilon$  is chosen 1 for a good approximation [44]. This energy functional is minimised to find the OD boundary.

GRADIENT DESCENT FLOW: The gradient descent method is used to minimise the approximated energy functional. For a fixed level set function  $\phi$ , functional Eq.(12) is minimised w.r.t the functions  $h_i^+$  and  $h_i^-$  for  $i = 1, 2, \dots, d$ . We obtain

$$h_i^+ = \frac{\kappa(x, y) * [H_\varepsilon(\phi(y)) I_i(y)]}{\kappa(x, y) * [H_\varepsilon(\phi(y))]} \quad (13)$$

$$h_i^- = \frac{\kappa(x, y) * [(1 - H_\varepsilon(\phi(y))) I_i(y)]}{\kappa(x, y) * [1 - H_\varepsilon(\phi(y))]} \quad (14)$$

Keeping  $h_i^+$  and  $h_i^-$  fixed and minimising the energy functional Eq.(12) w.r.t to  $\phi$ , the obtained gradient vector flow is:

$$\begin{aligned} \frac{\partial \phi}{\partial t} = & -\delta_\varepsilon(\phi)(e^+ - e^-) + \alpha \delta_\varepsilon(\phi) \operatorname{div} \left( \frac{\nabla \phi}{|\nabla \phi|} \right) \\ & + \beta \left( \nabla^2 \phi - \operatorname{div} \left( \frac{\nabla \phi}{|\nabla \phi|} \right) \right) \end{aligned} \quad (15)$$

where  $\delta_\varepsilon$  is the smooth Dirac function given in Eq.(11) and  $e^+$  and  $e^-$  are the functions below:

$$e^+(x) = \frac{1}{d} \sum_{i=1}^d \lambda_i^+ \int_{\Omega_y} \kappa(x, y) |I_i(y) - h_i^+|^2 dy$$

and

$$e^-(x) = \frac{1}{d} \sum_{i=1}^d \lambda_i^- \int_{\Omega_y} \kappa(x, y) |I_i(y) - h_i^-|^2 dy$$

where  $h_i^+$  and  $h_i^-$  are given by Eq.(13) and Eq.(14), respectively.

#### ACKNOWLEDGMENT

This work was supported by the Department of Science and Technology, Govt. of India, under Grant SR/S3/EECE/0024/2009. The authors would like to thank Dr. Kundan Karan and Dr. Prashanth R. for providing ground truth.

#### REFERENCES

- [1] W.H.O, "World health organization programme for the prevention of blindness and deafness- global initiative for the elimination of avoidable blindness," W.H.O: Document no.WHO/PBL/97.61 Rev.1; Geneva: 1997, 1997.
- [2] G. Michelson, S. Wrntges, J. Hornegger, and B. Lausen, "The papilla as screening parameter for early diagnosis of glaucoma," Deutsches Arzteblatt international, vol. 105, pp. 34–35, 2008.
- [3] R. Bock, J. Meier, L. G. Nyl, and G. Michelson, "Glaucoma risk index:automated glaucoma detection from color fundus images," Medical Image Analysis, vol. 14(3), pp. 471–481, 2010.
- [4] D. E. Singer, D. Nathan, H. A. Fogel, and A. P. Schachat, "Screening for diabetic retinopathy," Annals of Internal Medicine, vol. 116, pp. 660–671, 1992.
- [5] P. L. Rosin, D. Marshall, and J. E. Morgan, "Multimodal retinal imaging: New strategies for the detection of glaucoma," Proc. ICIP, 2002.
- [6] M.-L. Huang, H.-Y. Chen, and J.-J. Huang, "Glaucoma detection using adaptive neuro-fuzzy inference system," Expert Systems with Applications, vol. 32(2), pp. 458–468, 2007.
- [7] J. Meier, R. Bock, G. Michelson, L. G. Nyl, and J. Hornegger, "Effects of preprocessing eye fundus images on appearance based glaucoma classification," Proc. CAIP, pp. 165–172, 2007.
- [8] R. Bock, J. Meier, G. Michelson, L. G. Nyl, and J. Hornegger, "Classifying glaucoma with image-based features from fundus photographs," Proc. DAGM, pp. 355–364, 2007.
- [9] H. Ohwada, M. Daidoji, S. Shirato, and F. Mizoguchi, "Learning first-order rules from image applied to glaucoma diagnosis," Proc. Int. Conf. Artificial Intelligence: Topics in Artificial Intelligence, pp. 494–505, 1998.
- [10] L. G. Nyl, "Retinal image analysis for automated glaucoma risk evaluation," SPIE: Medical Imaging, vol. 7497, pp. 74 971C1–9, 2009.
- [11] A. R. McIntyre, M. I. Heywood, P. H. Artes, and S. S. R. Abidi, "Toward glaucoma classification with moment methods," Proc. CRV, pp. 265–272, 2004.
- [12] J. Yu, S. S. R. Abidi, P. H. Artes, and A. McIntyre, "Automated optic nerve analysis for diagnostic support in glaucoma," Proc. IEEE Symposium on Computer-Based Medical Systems, pp. 97 – 102, 2005.
- [13] C. Muramatsu, T. Nakagawa, A. Sawada, Y. Hatanaka, T. Hara, T. Yamamoto, and H. Fujita, "Determination of cup and disc ratio of optical nerve head for diagnosis of glaucoma on stereo retinal fundus image pairs," Proc. SPIE: Medical Imaging, pp. 72 603L–2, 2009.
- [14] J. Xu, O. Chutatape, E. Sung, C. Zheng, and P. Chew, "Optic disk feature extraction via modified deformable model technique for glaucoma analysis," Pattern Recognition, vol. 40(7), pp. 2063–2076, 2007.
- [15] M. B. Merickel, X. Wu, M. Sonka, and M. Abramoff, "Optimal segmentation of the optic nerve head from stereo retinal images," Proc. SPIE: Medical Imaging, vol. 6143, pp. 1031–1038, 2006.
- [16] M. D. Abrmoff, W. L. M. Alward, E. C. Greenlee, L. Shuba, C. Y. Kim, J. H. Fingert, and Y. H. Kwon, "Automated segmentation of the optic disc from stereo color photographs using physiologically plausible features," Investigative Ophthalmology and Visual Science, vol. 48, pp. 1665–1673, 2007.
- [17] A. Guesalag, P. Irrarrazabal, M. Guarini, and R. Ivarez, "Measurement of the glaucomatous cup using sequentially acquired stereoscopic images," Measurement, vol. 34(3), pp. 207–213, 2003.
- [18] E. Corona, S. Mitra, M. Wilson, T. Krile, and Y. H. K. P. Soliz, "Digital stereo image analyzer for generating automated 3-d measures of optic disc deformation in glaucoma," IEEE Trans Med Imaging, vol. 21(10), pp. 1244–1253, 2002.
- [19] D. Wong, J. Liu, J. H. Lim, H. Li, X. Jia, F. Yin, and T. Wong, "Automated detection of kinks from blood vessels for optic cup segmentation in retinal images," Proc. SPIE: Medical Imaging, p. 72601J, 2009.
- [20] G. D. Joshi, J. Sivaswamy, K. Karan, P. R., and R. Krishnadas, "Vessel bend-based cup segmentation in retinal images," Proc. Int. Conf. Pattern Recognition (ICPR), pp. 2536–2539, 2010.

- [21] N. Inoue, K. Yanashima, K. Magatani, and T. Kurihara, "Development of a simple diagnostic method for the glaucoma using ocular fundus pictures," *Proc. EMBS*, pp. 3355 – 3358, 2005.
- [22] Y. Hatanaka, A. Noudo, C. Muramatsu, A. Sawada, T. Hara, T. Yamamoto, and H. Fujita, "Automatic measurement of vertical cup-to-disc ratio on retinal fundus images," *Proc. ICMB*, pp. 64–72, 2010.
- [23] K. Stapor, A. Sacutewitonski, R. Chrastek, and G. Michelson, "Segmentation of fundus eye images using methods of mathematical morphology for glaucoma diagnosis," *Proc. ICCS*, pp. 41–48, 2004.
- [24] D. Wong, J. Liu, J. Lim, X. Jia, F. Yin, H. Li, and T. Wong, "Level-set based automatic cup-to-disc ratio determination using retinal fundus images in argali," *Proc. EMBC*, pp. 2266–2269, 2008.
- [25] J. Liu, D. Wong, J. Lim, H. Li, N. Tan, and T. Wong, "Argali- an automatic cup-to-disc ratio measurement system for glaucoma detection and analysis framework," *Proc. SPIE, Medical Imaging*, pp. 72 603K–8, 2009.
- [26] G. L. Spaeth, J. Henderer, C. Liu, M. Kesen, U. Altangerel, A. Bayer, L. J. Katz, J. Myers, D. Rhee, and W. Steinmann, "Disc damage likelihood scale:reproducibility of a new method of estimating the amount of optic nerve damage caused by glaucoma," *Trans Am Ophthalmol Soc.*, vol. 100, pp. 181–186, 2002.
- [27] N. Patton, T. M. Aslam, T. MacGillivray, I. J. Deary, B. Dhillon, R. H. Eikelboom, K. Yogesan, and I. J. Constable, "Retinal image analysis: Concepts, applications and potential," *Progress in Retinal and Eye Research*, vol. 25(1), pp. 99–127, 2006.
- [28] M. Lalonde, M. Beaulieu, and L. Gagnon, "Fast and robust optic disc detection using pyramidal decomposition and hausdorff-based template matching," *IEEE Trans Med Imaging.*, vol. 20(11), pp. 1193–1200, 2001.
- [29] R. Chrastek, M. Wolf, K. Donath, G. Michelson, and H. Niemann, "Optic disc segmentation in retinal images," *Proc. BVM*, pp. 263–266, 2002.
- [30] R. A. Abdel-Ghafar and T. Morris, "Progress towards automated detection and characterization of the optic disc in glaucoma and diabetic retinopathy," *Informatcs for Health and Social Care*, vol. 32(1), pp. 19–25, 2007.
- [31] P. Pallawala, W. Hsu, M. Lee, and K. Eong, "Automated optic disc localization and contour detection using ellipse fitting and wavelet transform," *Proc. ECCV*, pp. 139–151, 2004.
- [32] F. Mendels, C. Heneghan, and J. P. Thiran, "Identification of the optic disc boundary in retinal images using active contours," *Proc. IMVIP*, pp. 103–115, 1999.
- [33] A. Osareh, M. Mirmehdi, B. Thomas, and R. Markham, "Colour morphology and snakes for optic disc localisation," *Proc. MIUA*, pp. 21–24, 2002.
- [34] S. Lee and M. Brady, "Optic disk boundary detection," *Proc. BMVC*, pp. 359–362, 1991.
- [35] J. Lowell, A. Hunter, D. Steel, A. Basu, R. Ryder, E. Fletcher, and L. Kennedy, "Optic nerve head segmentation," *IEEE Trans. Medical Imaging*, vol. 23(2), pp. 256–264, 2004.
- [36] J. Novo, M. Penedo, and J. Santos, "Localisation of the optic disc by means of GA-optimised topological active nets," *Image and Vision Computing*, vol. 27(10), pp. 1572–1584, 2009.
- [37] H. Li and O. Chutatape, "Boundary detection of optic disk by a modified ASM method," *Pattern Recognition*, vol. 36(9), pp. 2093–2104, 2003.
- [38] —, "A model based approach for automated feature extraction in fundus images," *IEEE Transaction on Biomedical Engineering*, vol. 51(2), pp. 246–254, 2004.
- [39] T. Chan and L. Vese, "Active contours without edges," *IEEE Trans. Image Processing*, vol. 10(2), pp. 266–277, 2001.
- [40] D. Mumford and J. Shah, "Optimal approximation by piecewise smooth functions and associated variational problems," *Commun. Pure Appl. Math*, vol. 42, pp. 577–685, 1989.
- [41] G. D. Joshi, J. Sivaswamy, K. Karan, and R. Krishnadas, "Optic disk and cup boundary detection using regional information," *Proc. IEEE International Symposium on Biomedical Imaging (ISBI)*, pp. 948–951, 2010.
- [42] Y. Tang, X. Li, A. von Freyberg, and G. Goch, "Automatic segmentation of the papilla in a fundus image based on the C-V model and a shape restraint," *Proc. ICPR*, pp. 183–186, 2006.
- [43] S. Lankton and A. Tannenbaum, "Localizing region-based active contours," *IEEE Trans Image Process.*, vol. 17(11), pp. 2029–2039, 2008.
- [44] L. Wang, L. He, A. Mishra, and C. Li, "Active contours driven by local gaussian distribution fitting energy," *Signal Processing*, vol. 89(12), pp. 2435–2447, 2009.
- [45] C. Sagiv, N. A. Sochen, and Y. Y. Zeevi, "Integrated active contours for texture segmentation," *IEEE Transactions on Image Processing*, vol. 15(6), pp. 1633–1646, 2006.
- [46] T. F. Chan, B. Y. Sandberg, and L. A. Vese, "Active contours without edges for vector-valued images," *Journal of Visual Communication and Image Representation*, vol. 11(2), pp. 130–141, 2000.
- [47] R. O. Duda and P. E. Hart, "Use of the hough transformation to detect lines and curves in pictures," *Communications of the ACM*, vol. 15(1), pp. 11–15, 1972.
- [48] S. Garg, J. Sivaswamy, and S. Chandra, "Unsupervised curvature-based retinal vessel segmentation," *Proc. ISBI*, pp. 344–347, 2007.
- [49] C. Schmid, "Constructing models for content-based image retrieval," *Proc. CVPR*, vol. 2, pp. 39–45, 2001.
- [50] E. Ricci and R. Perfetti, "Retinal blood vessel segmentation using line operators and support vector classification," *IEEE Trans. Med. Imag.*, vol. 26(10), p. 13571365, 2007.
- [51] X. C. He and N. H. C. Yung, "Curvature scale space corner detector with adaptive threshold and dynamic region of support," *International Conference on Pattern Recognition*, pp. 791–794, 2004.